Journal of $CO_2$ Utilization 39 (2020) 101143

Contents lists available at ScienceDirect

Journal of $CO_2$ Utilization

journal homepage: www.elsevier.com/locate/jcou

# Selective adsorption of $CO_2/CH_4$ mixture on clay-rich shale using molecular simulations

Yueliang Liu[a,b,*], Jian Hou[a,b]

[a] Key Laboratory of Unconventional Oil & Gas Development, China University of Petroleum (East China), Ministry of Education, Qingdao, 266580 China
[b] School of Petroleum Engineering, China University of Petroleum (East China), Qingdao, Shandong, 266580 China

ARTICLE INFO

*Keywords:*
Adsorption selectivity
Montmorillonite-rich
Gas-bearing reservoirs
$CO_2$ sequestration
$CH_4$ recovery

ABSTRACT

Shale rocks comprise of a lager proportion of clay minerals; shale gas potentially adsorbs on the clay minerals due to its large specific surface area. In this work, selective adsorption behaviors of $CO_2/CH_4$ are investigated in clay-mineral nanopores using the grand canonical Monte Carlo (GCMC) simulation method. In addition, the subsequent implications for $CH_4$ recovery and $CO_2$ sequestration are summarized. Results show that $CH_4$ exhibits the strongest adsorption on kaolinite, followed by that on illite and montmorillonite, while adsorption capacity of $CO_2$ is calculated in the order of montmorillonite > illite ≈ kaolinite, suggesting that $CO_2$ injection has the best performance for $CH_4$ recovery when implemented in montmorillonite-rich shale reservoirs. Comparatively, smaller pores are dominated by the adsorbed gas and are also favorable for $CO_2$ sequestration. The adsorption selectivity of $CO_2$ over $CH_4$ on clay minerals is predicted in the order of kaolinite < illite < montmorillonite; moreover, the adsorption selectivity is reduced as pressure decreases for illite and montmorillonite, implying that the injection pressure of $CO_2$ should be low enough to achieve an efficient $CH_4$ recovery and $CO_2$ sequestration. However, the ideal injection pressure of $CO_2$ should be around the pressure where it has the maximum adsorption selectivity for kaolinite-rich shale. This study may achieve a deeper understanding of the adsorption behavior of $CO_2/CH_4$ in clay-rich gas-bearing reservoirs; furthermore, it may provide the guidelines for future optimization design of $CO_2$ injection for $CH_4$ recovery and $CO_2$ sequestration in the field applications.

## 1. Introduction

With an increasing demand for fossil fuels, shale gas is accepted as an important substitute for conventional fossil resources, owning to its huge reserves and potential $CO_2$ sequestration [1–4]. Generally, shale-gas storage in shale matrix exists in three patterns, i.e., adsorbed gas on rock surface (a dense and liquid-like phase), dissolved gas in organic matter, and free gas existing in pore networks [5–7]. With the gas storage in a dense and liquid-like adsorbed state, the overall gas-storage capacity is greatly improved relative to that in a free state alone [8]. Based on the characteristics of gas-bearing reservoirs, the volume proportion of adsorbed gas accounts for a sizeable shale of the total reserves in five US shale formations, ranging from 20 vol% to 85 vol% [9]. In addition, the adsorbed gas could occupy more than 50 % of the total gas reserves in the Devonian shales [10]. $CO_2$ injection has been recognized as a viable strategy for $CH_4$ recovery, along with the potential $CO_2$ sequestration [11–18]. A better understanding of $CO_2/CH_4$ adsorption is responsible for sustainable shale gas production; and, more importantly, it provides the basic guidelines for optimizing $CO_2$ injection on site for realizing $CH_4$ recovery and $CO_2$ sequestration.

The selective adsorption between $CH_4$ and $CO_2$ is heavily investigated to shed light on the mechanism of shale gas recovery using $CO_2$ injection method. Previously, the $CH_4$ and $CO_2$ adsorption were extensively measured on shale samples; it was found that $CO_2$ presents the adsorption capacity more than five times greater than $CH_4$, evaluating the potential of $CO_2$ for enhanced $CH_4$ recovery [19,20]. Moreover, adsorption of $CO_2$, $CH_4$ were measured on Sichuan basin shale by Duan et al. [21], and they also observed the much higher adsorption capacity of $CO_2$ than $CH_4$. However, $CO_2$ and $CH_4$ are generally mingled coming into being gas mixtures, which usually exhibits selective adsorption on shale. Ortiz Cancino et al. [22] measured the adsorption of an equal molar mixture of $CO_2/CH_4$ on black shale samples. The measured high adsorption selectivity of $CO_2$ over $CH_4$ highlights the more affinity of $CO_2$ to the organic matter in shale.

Typically, shale rocks mainly comprise organic, such as kerogen, and inorganic matter, such as clay minerals, calcite and quartz. In shale reservoirs, clay minerals in inorganic matter and organic matter are two major controlling factors accounting for gas adsorption [23]. Lately, the

* Corresponding author at: Petroleum Engineering, China University of Petroleum (East China), China.
*E-mail address:* sdliuyueliang@163.com (Y. Liu).

https://doi.org/10.1016/j.jcou.2020.02.013
Received 21 October 2019; Received in revised form 3 February 2020; Accepted 20 February 2020
Available online 13 March 2020

influences of organic substance content, kerogen type and thermal maturity on gas-adsorption has been studied extensively [24]. It was found the gas adsorption capacity linearly correlates with the total content of organic matter; meanwhile, high vitrinite accounts for the stronger gas adsorption on shale [25,26]. In addition, clay mineral composition as well as its micropore structure also exert influences in affecting the gas adsorption owning to their large specific surface area by providing the adsorption sites for natural gas [27]. Lu et al. [28] performed adsorption measurements on core samples in Devonian shale; they found that the presence of illite was responsible for adsorption and gas storage, especially for samples with little content of organic matter. In addition, laboratory experiments were performed by Ross and Bustin [29] to explore the influences of clay minerals, especially montmorillonite and illite, on the storage capacity in shale reservoirs. They deduced that gas adsorption depends on the clay mineral types and the micropore structures of the clay platelets [29]. Summarily, these studies conducted on shale samples, however, cannot reasonably address the influence of clay minerals on gas adsorption due the co-existence of organic matter. Future studies should be performed to investigate the fundamental mechanisms of the separate effects of typical clay minerals on $CO_2/CH_4$ adsorption.

Experimental measurements are inevitably sophisticated and generally need complex data-interpretation procedures. By contrast, due to its powerful computational capacity, molecular simulation method is thereby employed as an alternative of the experimental measurement to gain sights into the micro-adsorption behaviors of $CO_2/CH_4$ in shale systems [30–36]. Due to presence of organic matter in shale, attempts were employed to explore the selective adsorption of $CO_2/CH_4$ mixture in organic nanopores using molecular simulations [33,34,37–46]. Traditionally, graphic and carbon-slit pores are generally used in previous studies to simulate the organic pores in shale [39,41]. However, these simple carbon-like pores cannot really simulate the natural properties of organic matter in shale. Most recently, studies were conducted to reveal the fundamental mechanisms of $CO_2/CH_4$ adsorption on realistic organic matter using molecular simulation methods. For example, Sun et al. [44] used molecular simulations to investigate the adsorption of $CO_2/CH_4$ in organic nanopores; based on their predicted results, the replacement efficiency of $CO_2$ was thereby calculated for $CH_4$ recovery from organic pores. Moisture may play a key role in affecting adsorption of $CO_2/CH_4$ on shale. Using GCMC simulations, Huang et al. [33] implemented investigation on the influence of moisture content on the selective adsorption of $CO_2/CH_4$ on kerogen; a negative effect of the water content was reported to gas adsorption on organic nanopores [33]. In spite of the previous studies, researches concerning $CO_2$ injection into clay-rich shales for $CH_4$ recovery and $CO_2$ storage is still at a preliminary stage and the underlying mechanisms of $CO_2/CH_4$ adsorption in clay nanopores are still scarcely reported.

Here, in this work, three typical clay-mineral models. i.e., illite, montmorillonite, kaolinite, are developed using the GCMC simulation method. This method is first validated by comparing the predicted $CO_2/CH_4$ adsorption with the measured adsorption data. Adsorption behavior of $CO_2/CH_4$ in clay-mineral nanopores is then predicted under different reservoir conditions; specifically, the influencing factors, i.e., system pressure, temperature and pore size, are comprehensively discussed from the micropore-scale perspective. Furthermore, we have a deep discussion on the potential implications of $CO_2$ injection for $CH_4$ recovery and $CO_2$ sequestration by calculating the adsorption selectivity of $CO_2/CH_4$ in the clay-mineral pores. This study is useful for addressing the following questions: 1) can molecular simulation reasonably represent the adsorption behavior of gas mixtures on clay minerals? 2) how does the $CO_2/CH_4$ adsorption behave in different clay-mineral pores? 3) how to reasonably optimize $CO_2$ injection to achieve successful $CO_2$ sequestration and $CH_4$ recovery in clay-rich shales with the knowledge of $CO_2/CH_4$ adsorption on clay-minerals? This study helps gain a deep insight into the adsorption behavior of $CO_2/CH_4$ in clay-rich gas-bearing reservoirs; more importantly, it provides the guidelines for future optimization design of $CO_2$ injection for $CH_4$ recovery and $CO_2$ sequestration in the field applications.

## 2. Molecular models and simulations

### 2.1. Molecular clay-mineral models

Based on the X-ray diffraction (XRD) analyses, illite, montmorillonite and kaolinite are three dominating clay minerals in Longmaxi shale samples derived from Sichuan Basin of China [41,42]. According to surface morphology of the Longmaxi shale, shape morphology of the mineral pores in illite, montmorillonite and kaolinite is simplified as slit-shaped.

Illite is one typical 2:1 clay mineral in shale, which is consisted of one Al-O octahedral sheet located between two Si-O tetrahedral sheets [47]. In this study, the illite is represented with the general unit cell formula of $K_x[Al_xSi_{(8-x)}][Al_yMg_{4-y}]O_{20}(OH)_4$ [48], where $x$ and $y$ are set as 1 and 4, respectively, for each unit cell. In every unite cell, one $Si^{4+}$ is only replaced by only one $Al^{3+}$, resulting in negative charged clay sheets. $K^+$ cations are randomly distributed between the interlayers, counterbalancing the induced electrostatic charges in the unit cell. Notes that $K^+$ cations are mobile in the simulation cell. The parameters of each unit cell are selected as $a$ = 0.516 nm, $b$ = 0.935 nm, $\alpha$ = 91.03°, $\beta$ = 100.37°, $\gamma$ = 89.75° [49,50]. The simulation cell contains two clay sheets, wherein each sheet consists of 24 unit cells (6 × 4×1 supercell). The simulation cell thereby has the dimension of 3.096 nm × 3.740 nm in the $x$ and $y$ directions, respectively. The illite nanopores are represented by two clay sheets separated with a fixed distance. Fig. 1**(a)** presents the schematic structure of the illite nanopore. Pore width is calculated as the separation between the centers of two opposite oxygen atoms in the inner layers of the two clay sheets.

Montmorillonite is a 2:1 cationic mineral in shale, which is comprised by two Si-O sheets and one Al-O sheet [51]. The simulation cell contains two clay sheets, wherein each sheet consists of 24 unit cells (6 × 4 × 1 supercell). The simulation cell has the dimension of 3.168 nm × 3.656 nm in the $x$ and $y$ directions, respectively. Within the supercell, one $Al^{3+}$ atom in every eight $Al^{3+}$ atoms are homogeneously substituted by $Mg^{2+}$ in the octahedral sheet; moreover, one $Si^{4+}$ atom in every 32 atoms are replaced by $Al^{3+}$ atoms in the tetrahedral sheet [52], resulting in negative charged clay sheets. The negative charge is counterbalanced by introducing $Na^+$ cations which are randomly distributed between the interlayers, resulting in Na-montmorillonite with the formula of $Na_{0.75}(Al_{0.25}Si_{7.75})(Al_{3.5}Mg_{0.5})O_{20}(OH)_4$. The montmorillonite nanopores are represented by two clay sheets separated with a fixed distance, of which the pore width is calculated as the separation between the centers of two opposite oxygen atoms in the inner layers of the two clay sheets. Fig. 1**(b)** presents the schematic structure of the montmorillonite nanopore.

Kaolinite is a 1:1 clay mineral, which is consisted of one Al-O octahedral sheet and one Si-O tetrahedral sheet. The parameters of the unite cell are set as $a$ = 0.5154 nm, $b$ = 0.8942 nm, $c$ = 0.7391 nm, $\alpha$ = 91.92°, $\beta$ = 105.05°, $\gamma$ = 89.90° [53], resulting in the formula of $Al_4Si_4O_{10}(OH)_8$ [53]. Each sheet consists of 24 unit cells (6 × 4×1 supercell), resulting a dimension of 3.0924 nm × 3.5768 nm in the $x$ and $y$ directions, respectively. The kaolinite nanopores are represented by two clay sheets separated with a fixed distance, of which the pore width is calculated as the separation between the centers of two opposite hydrogen atoms in the two clay sheets. Fig. 1**(c)** presents the schematic structure of the kaolinite nanopore. It is noted that the equilibrium occurs at a point where the adsorption and desorption have the same grand potential values.

### 2.2. Force field parameters

The potential models used for $CH_4$ and $CO_2$ molecules are obtained from the TraPPE force filed [54], while the CLAYFF force field is

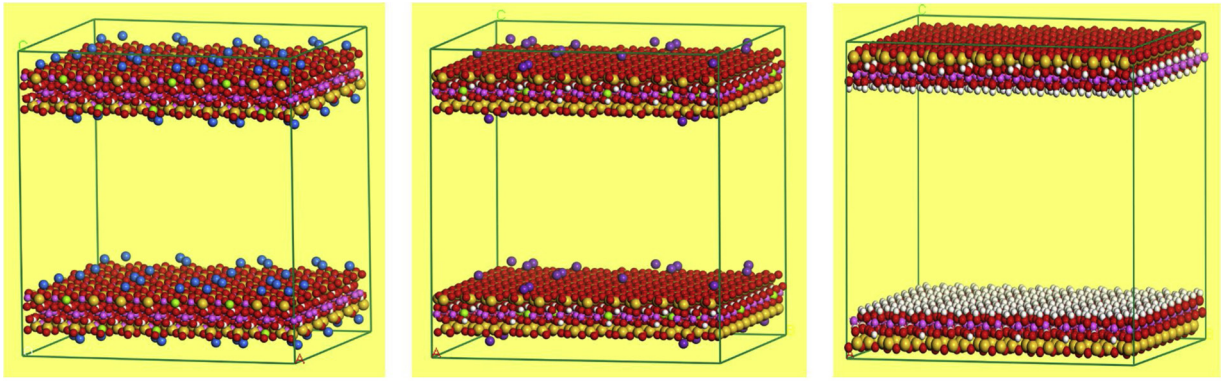


**Fig. 1.** Schematic structures of the clay-mineral nanopores: (a) K-illite; (b) Na-montmorillonite; and (c) kaolinite. Red spheres represent O atoms, pink spheres represent Al atoms, green spheres represent Mg atoms, yellow spheres represent Si atoms, white spheres represent H atoms, blue spheres represent $K^+$ ions and cyan spheres represent $Na^+$ ions.

applied for the clay models. In a $CH_4$ molecule, the C atom and the H atom are treated as a united atom. As for a $CO_2$ molecule, the partial charge of the C atom and O atom are +0.7 e and -0.35 e, respectively. The CLAYFF model has been extensively applied to investigate the thermodynamic as well as the static properties of fluids in clay minerals, which presents an excellent agreement with the experimental data [55]. The nonbonded interactions include Lennard-Jones (LJ) and electrostatic terms, which are described by the following potential model,

$$u(r_{ij}) = 4\varepsilon_{ij}\left[\left(\frac{\sigma_{ij}}{r_{ij}}\right)^{12} - \left(\frac{\sigma_{ij}}{r_{ij}}\right)^{6}\right] + \frac{q_i q_j}{4\pi\varepsilon_0 r_{ij}} \tag{1}$$

where $r_{ij}$ represents the separation distance between the atoms $i$ and $j$; $\varepsilon_{ij}$ and $\sigma_{ij}$ represent the well depth of $LJ$ potential and the $LJ$ radius, respectively; $q$ is the atrial atom charge to calculate the Coulomb interactions. The Lorentz-Berthelot combining rules are used to calculate the cross interactions between two different atoms [56],

$$\sigma_{ij} = \frac{1}{2}(\sigma_{ii} + \sigma_{jj}) \tag{2}$$

$$\varepsilon_{ij} = \sqrt{\varepsilon_{ii}\varepsilon_{jj}} \tag{3}$$

The cutoff radius is set as 1.25 nm. In order to take the long-range electrostatic interactions into consideration, a vacuum slab is placed in the $z$ direction in the simulation cell, which is estimated with the Ewald summation method [57,58].

### 2.3. Simulation details

In this work, GCMC simulations are applied to explore adsorption behavior of the $CO_2/CH_4$ mixture in the clay-mineral nanopores under shale reservoir conditions. This work is performed in the grand canonical $\mu VT$ ensemble; it is noted that within such an ensemble, the chemical potentials ($\mu$), system volume ($V$) and temperature ($T$) are kept as constant [59]. Within the framework of the GCMC simulations, gas molecules confined in the clay-mineral pores can exchange with a fictitious bulk gas reservoir; such a reservoir is set with a fixed chemical potential. Notes that the chemical potentials are computed using the Peng-Robinson equation of state [60]. An equal probability is endowed to the gas molecules, which can be inserted or removed from the confined nanopores depending on the chemical potential of the fictitious gas reservoir. This simulation comprises of 0.2 million cycles for each molecule to achieve equilibrium and 0.7 million cycles for sampling fluid distribution in nanopores.

The excess adsorption is computed by deducting the total amount of gas, which occupies the entire pore volume and is endowed with the bulk density, from the total gas loading [33,57],

$$\Gamma_{ex} = \frac{\langle N_{ab}\rangle}{N_A} - \frac{\rho_{bulk} V}{M} \tag{4}$$

where $\Gamma_{ex}$ represents the amount of excess adsorption, kmol/m$^3$; $\langle N_{ab}\rangle$ represents the total amount of gas residing in clay-mineral pores; $N_A$ represents Avogadro constant, $6.022 \times 10^{23}$; $M$ represents molecular weight, g/mol. $V$ represents the effective pore volume. $\rho_{bulk}$ denotes the bulk gas density according to the National Institute of Standards and Technology (NIST) Chemistry WebBook, g/cm$^3$.

The excess adsorption calculation highly depends on the determination of the effective pore volume. Based on the volumetric method, the effective pore volume is determined from the helium adsorption by assuming that helium adsorption is negligible in nanopores and the total uptake is dominated by the mechanism of pore filling [61]. It has been reported that the pore volume of different clay-mineral pores can remain in a constant value in a wide temperature and pressure range [62]; we thereby calculate the effective pore volume using the helium adsorption as,

$$V_p = \frac{\langle N_{He}\rangle}{N_A \rho^{molar}_{He,bulk}} \tag{5}$$

where $\langle N_{He}\rangle$ is the average molecular numbers of helium in nanopores; $\rho^{molar}_{He,bulk}$ represents the molar density of helium in bulk; and $N_A$ represents Avogadro constant. It is found that the effective pore volume is independent on the system pressure and temperature, while it increases linearly with slit aperture. In addition, the effective pore volume is less than that obtained by simply multiplying the surface area with the slit aperture due to the finite molecular size of helium [61].

The adsorption selectivity of $CO_2$ over $CH_4$ is calculated to characterize the selective adsorption behavior of $CO_2/CH_4$ mixture in clay nanopores, which is calculated as [63],

$$S_{CO_2/CH_4} = \frac{(x_{CO_2}/x_{CH_4})}{(y_{CO_2}/y_{CH_4})} \tag{6}$$

where $x_{CO2}$ and $x_{CH4}$ represent the molar fractions of $CO_2$ and $CH_4$ in the clay nanopores, respectively; $y_{CO2}$ and $y_{CH4}$ represent the molar fractions of $CO_2$ and $CH_4$ in the bulk gas reservoir. If $S_{CO2/CH4}$ is larger than unit, it suggests that $CO_2$ is more inclined to adsorb on the clay surface than $CH_4$ [64].

## 3. Adsorption measurement

Thermogravimetric method is applied to measure the excess

adsorption of $CH_4$ and $CO_2$ on the three clay minerals. The purities of $CO_2$ and $CH_4$ are 99.50 mol% and 99.00 mol%, respectively. It should be noted that the key part in the thermogravimetric adsorption apparatus is a magnetic suspension balance. It enables the adsorption apparatus to measure the weight difference down to ± 2.0 μg, which is thereby more accurate than the traditional volumetric method. More details of the thermogravimetric method can be inferred in our previous works [59]. The operating temperatures are selected as 303.15 K, 333.15 K and 363.15 K, respectively, while the operating pressures are up to 350 bar.

## 4. Results and discussion

In this section, the GCMC simulation method is first validated by comparing with the experimental data. It is then applied to explore the adsorption behavior of $CO_2/CH_4$ mixture on clay-mineral pores. Based on the adsorption results, the potential implications of $CO_2$ sequestration and $CH_4$ recovery are discussed.

### 4.1. Validation of the GCMC method

The excess adsorption of $CO_2/CH_4$ mixture (50.0 mol%:50.0 mol%) are measured on the three clay minerals using the thermogravimetric method. The thermogravimetric method can be inferred in our previous works [59]. In addition, the three clay minerals are montmorillonite, illite and kaolinite, which are pure powder samples. The measured data is then compared with that predicted results from the GCMC simulations to validate its efficiency in calculating $CO_2/CH_4$ adsorption on clay minerals, as shown in Figs. 2–3. It should be noted that the $CO_2/CH_4$ mixture with the same composition is built in the GCMC simulation; meanwhile, the adsorption of $CO_2/CH_4$ mixture is simulated in the three clay mineral pores to mimic the experimental measurement.

The calculated excess adsorption of $CO_2/CH_4$ mixture on the three clay minerals does not fit perfectly well with the measured adsorption data, especially as higher-pressure conditions. However, the magnitude of excess adsorption of $CO_2/CH_4$ mixture is fairly close to the experimental results. As shown in Fig. 2, the deviation between the experimental and simulation results is larger at 303.15 K, indicating that the GCMC simulation method exhibits less efficiency at low temperature conditions. Fig. 3 presents that the calculated excess adsorption of $CO_2/CH_4$ mixture show the highest capacity on montmorillonite, followed by illite and kaolinite, at the same temperature/pressure conditions, which is consistent with the measured adsorption isotherms. The difference between the measured and simulated adsorption is probably resulted from the issue of pore accessibility [65–70]; specifically, due to the presence of impenetrable pore necks between theoretically enterable pores, adsorbates generally have the pore accessibility problems into the realistic heterogeneous porous materials, such as shale and clay samples [71]. Based on the statistical analysis, the relative deviations between the calculated and the experimental results are within an acceptable range of 0–5.25 %, validating our GCMC simulations in predicting excess adsorption of $CO_2/CH_4$ mixture under shale reservoir conditions.

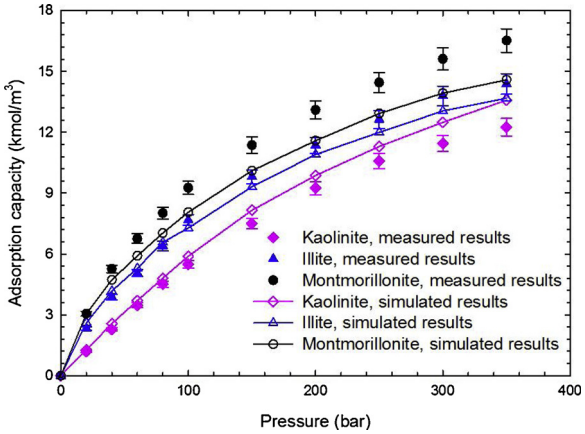


**Fig. 3.** Adsorption capacities of $CO_2/CH_4$ (50.0 mol%:50.0 mol%) mixture on montmorillonite, illite and kaolinite at 333.15 K.

### 4.2. $CH_4/CO_2$ adsorption on clay minerals

#### 4.2.1. Effect of system pressure

Figs. 4–6 present the density profiles of $CO_2/CH_4$ (50.0 mol%:50.0 mol%) in the 3-nm clay-mineral pores at different pressures. In the first place, the density near the pore surface formed by $CO_2$ is significantly higher than that by $CH_4$, suggesting the much stronger adsorption capacity and the more affinity of $CO_2$ in clay nanopores. More interestingly, $CH_4$ performs the highest adsorption capacity on kaolinite, accompanying with the formation of stronger adsorption layers on pore surface. On the contrary, the adsorption capacity of $CO_2$ on clay minerals are calculated in the order of montmorillonite > illite ≈ kaolinite. That is, montmorillonite has the highest adsorption to $CO_2$ but the smallest adsorption capacity to $CH_4$. It implies that as for montmorillonite-rich shale, $CO_2$ injection could be a more efficient approach for $CH_4$ recovery compared to illite- and kaolinite-rich shale reservoirs. Kaolinite consists of one Al-O octahedral sheet and one Si-O tetrahedral sheet; $CH_4$ molecules tend to be more attracted on kaolinite due to the stronger fluid-fluid interactions compared to that on illite and montmorillonite. However, the interaction between kaolinite and $CO_2$ molecules is weaker than that on illite and montmorillonite, resulting in

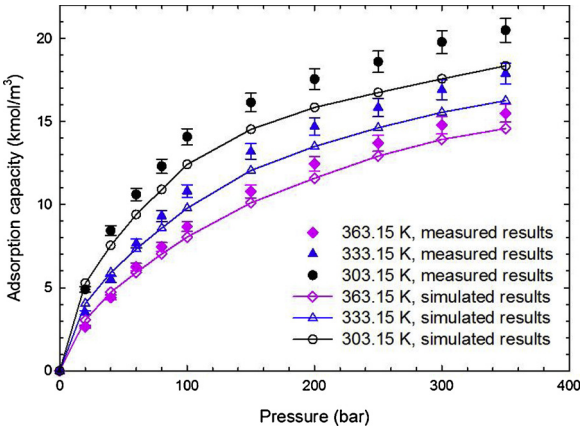


**Fig. 2.** Adsorption capacities of the $CO_2/CH_4$ (50.0 mol%:50.0 mol%) mixture on montmorillonite.

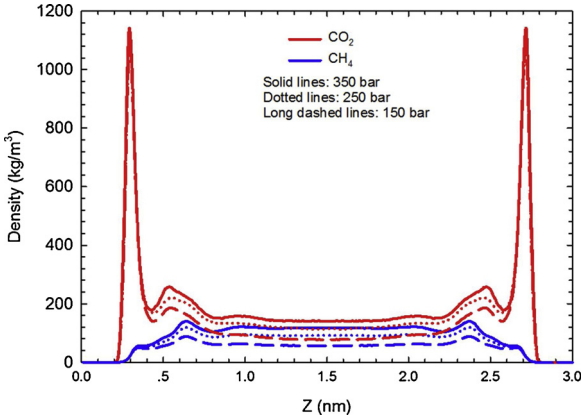


**Fig. 4.** Density profiles of $CO_2/CH_4$ (50.0 mol%:50.0 mol%) at 363.15 K in the 3-nm illite pore.

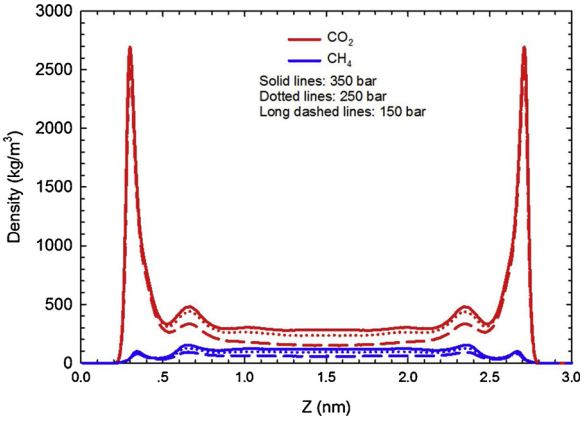


**Fig. 5.** Density profiles of $CO_2/CH_4$ (50.0 mol%:50.0 mol%) at 363.15 K in the 3-nm montmorillonite pore.

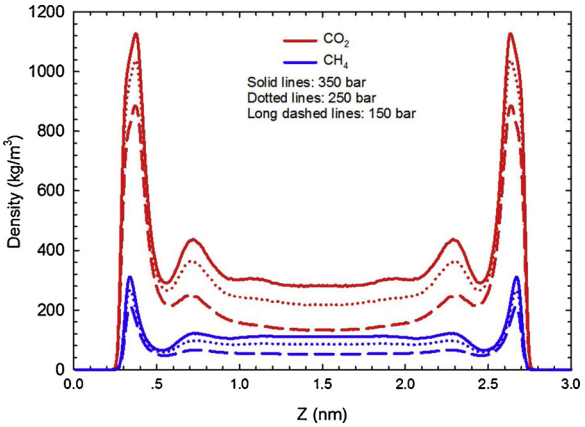


**Fig. 6.** Density profiles of $CO_2/CH_4$ (50.0 mol%:50.0 mol%) at 363.15 K in the 3-nm kaolinite pore.

the less adsorption on kaolinite.

Moreover, as shown in Figs. 4–6, density of $CO_2$ near the pore surface is reduced with the decreasing pressure in the kaolinite nanopores, suggesting that $CO_2$ adsorption on kaolinite is sensitive to reservoir pressures; by contrast, the $CO_2$ density near the pore surface is slightly affected by the pressure change in the illite and montmorillonite nanopores, indicating the less sensitivity of $CO_2$ to pressure on illite and montmorillonite. In addition, $CH_4$ adsorption on clay minerals is closely correlated with the reservoir pressure, indicated by the decrement of $CH_4$ density near the pore surface with the decreasing pressure. From this view, it is inferred that $CO_2$ injection could be most efficient for $CH_4$ recovery in the montmorillonite-rich shale gas reservoir, while it is the least efficient for kaolinite-rich shale reservoirs.

#### 4.2.2. Effect of system temperature

Figs. 7–9 present the density profiles of $CO_2/CH_4$ (50.0 mol%:50.0 mol%) in the 3-nm clay-mineral pores at 300 bar. Besides the adsorption layer formed near the pore surface, a second adsorption layer is also resulted from $CO_2$ adsorption in the clay-mineral nanopores. As system temperature decreases, the averaged density of $CO_2$ and $CH_4$ is reduced in the clay-mineral pores, indicating that adsorption of $CO_2$ and $CH_4$ is affected by the reservoir temperature. During shale reservoir development, reservoir temperature is generally kept as constant; the influence of temperature on shale gas production is thus rarely considered in previous works [72]. However, adsorption/desorption of shale gas during exploration is a dynamic process, accompanying with heat produce and release, which exerts a big impact on the reservoir temperature. It is thereby essential for revealing the effect of

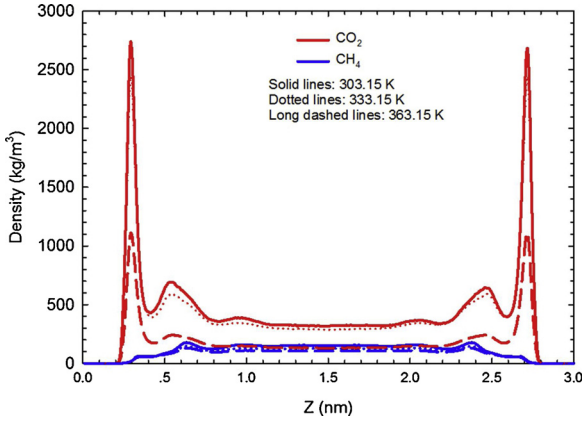


**Fig. 7.** Density profiles of $CO_2/CH_4$ (50.0 mol%:50.0 mol%) in the 3-nm illite pore at 300 bar.

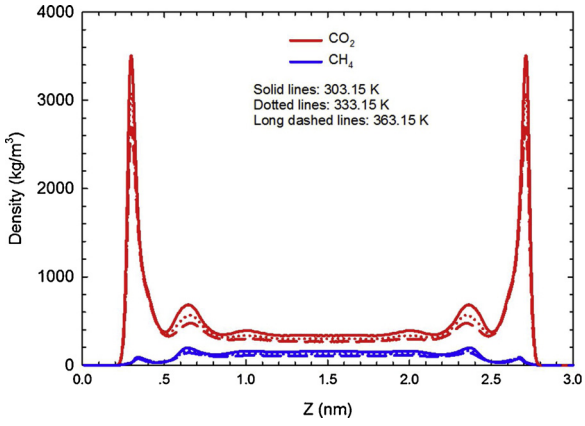


**Fig. 8.** Density profiles of $CO_2/CH_4$ (50.0 mol%:50.0 mol%) in the 3-nm montmorillonite pore at 300 bar.

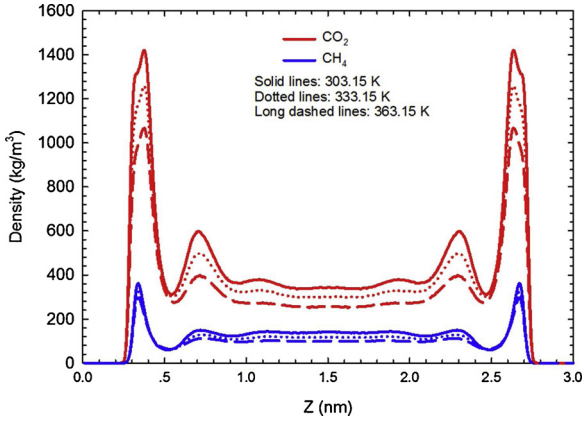


**Fig. 9.** Density profiles of $CO_2/CH_4$ (50.0 mol%:50.0 mol%) in the 3-nm kaolinite pore at 300 bar.

temperature on the adsorption behavior of $CO_2/CH_4$ mixture on shale.

#### 4.2.3. Effect of pore size

One unique characteristic of shale reservoirs is heterogeneity, where pores in shale matrix exhibit pore size distributions. Previously, extensive studies were conducted to reveal the adsorption behavior of shale gas in single nanopores. We thus investigate the adsorption behavior of $CO_2/CH_4$ mixture in clay-mineral pores with different pore sizes. Figs. 10–12 present the density profiles of $CO_2/CH_4$ (50 mol%:50 mol%) mixture in 1-nm and 3-nm pores, which are comprised of

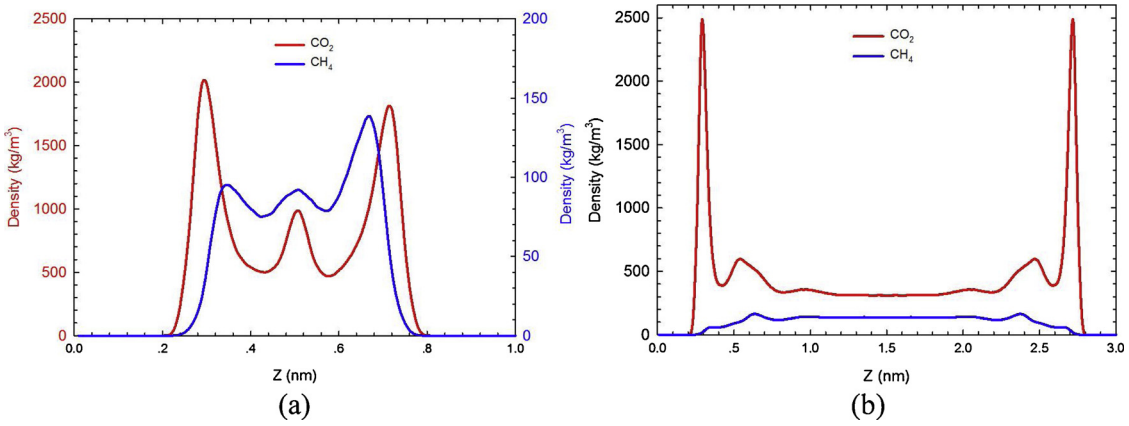


**Fig. 10.** Density profiles of $CO_2/CH_4$ (50.0 mol%:50.0 mol%) in the (a) 1-nm and (b) 3-nm illite pores at 333.15 K and 350 bar.

different clay minerals, i.e., illite, montmorillonite and kaolinite, respectively. We observe that the maximum adsorption density of $CH_4$ in the 1-nm pores is almost the same as that in the 3-nm pores. However, the maximum adsorption density of $CO_2$ in the 3-nm pores, comprised of montmorillonite and kaolinite, is remarkably higher than that in the 1-nm pores. From this view, $CO_2$ is superior in the large pores to that in the small pores for $CH_4$ recovery.

As shown in Figs. 10–12, density in the center of 1 nm pore is generally higher than that of the 3 nm pore due to the coupling effect from both sides of pore walls. In addition, a second adsorption layer comes into being in the 1-nm illite pore by $CO_2$ and $CH_4$ molecules. As shown in Fig. 10, quite interestingly, the adsorption layers formed by $CO_2$ and $CH_4$ are not equally distributed in both sides of the 1-nm illite pore; moreover, the formed adsorption layers by $CO_2$ are complementary to that by $CH_4$ molecules. On the contrary, we did not observe such asymmetric adsorption behavior in montmorillonite and kaolinite pores. This unique adsorption behavior occurred in illite is possibly caused by the preferential adsorption between $CH_4$ and $CO_2$ molecules on the negative charged pore surfaces when pore size is lower than certain value. In addition, the adsorption layers formed in the 1-nm pores are thicker than those formed in the 3-nm pores. In other words, the adsorbed state gas tends to dominate in the smaller clay nanopores, which are thereby the ideal space for $CO_2$ sequestration. As for clay-rich shale gas reservoirs, we should pay heavy attention to how to efficiently recover the adsorbed gas reserves from the smaller pores.

### 4.3. Implications for $CH_4$ recovery and $CO_2$ sequestration

Adsorption of $CO_2/CH_4$ mixture in clay-mineral pores closely correlates the implications of $CO_2$ injection for $CH_4$ recovery and $CO_2$ sequestration under shale reservoir conditions. In this section, the results obtained from the previous sections are used to analyze the implication potentials of $CH_4$ recovery and $CO_2$ sequestration in clay-rich shale reservoirs. Figs. 13–15 present the adsorption selectivity of $CO_2/CH_4$ (50.0 mol%:50.0 mol%) in the 3-nm clay-mineral pores. It is reported that the most important criteria for $CO_2$ sequestration is whether the buried $CO_2$ can realize the long-time storage underground or not [73]. As shown in Figs. 13–15, illite and montmorillonite present higher adsorption selectivity than kaolinite at the same pressure and temperature conditions; it implies that the adsorption capacity of $CO_2$ relative to $CH_4$ is stronger on illite and montmorillonite than that on kaolinite. Such a high adsorption capacity of $CO_2$ on the clay minerals facilitates $CO_2$ sequestration for a long-time storage in shale gas reservoir, while the relatively higher adsorption of $CO_2$ to $CH_4$ enables $CO_2$ a much high efficiency for $CH_4$ recovery. Illite and montmorillonite are thereby adopted as the optimized clay mineral types for $CO_2$ sequestration and $CH_4$ recovery in the field applications.

Understanding of the effect of pressure on selective adsorption of $CO_2$ over $CH_4$ can provide the basic guidance for $CO_2$ injection with the implications of $CO_2$ sequestration and $CH_4$ recovery. Results show that the selective adsorption of $CO_2$ over $CH_4$ decreases in the illite and montmorillonite pores as reservoir pressure increases. However, as for kaolinite pores, the adsorption selectivity is generally larger at lower pressure conditions, and there is an optimum pressure (around 70 bar) for the maximum adsorption selectivity. Previous works also observed

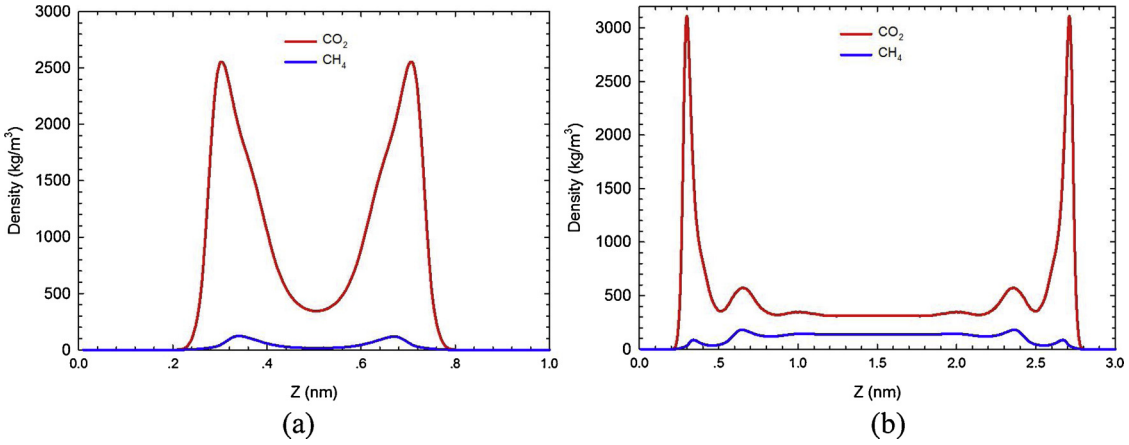


**Fig. 11.** Density profiles of $CO_2/CH_4$ (50.0 mol%:50.0 mol%) in the (a) 1-nm and (b) 3-nm montmorillonite pores at 333.15 K and 350 bar.

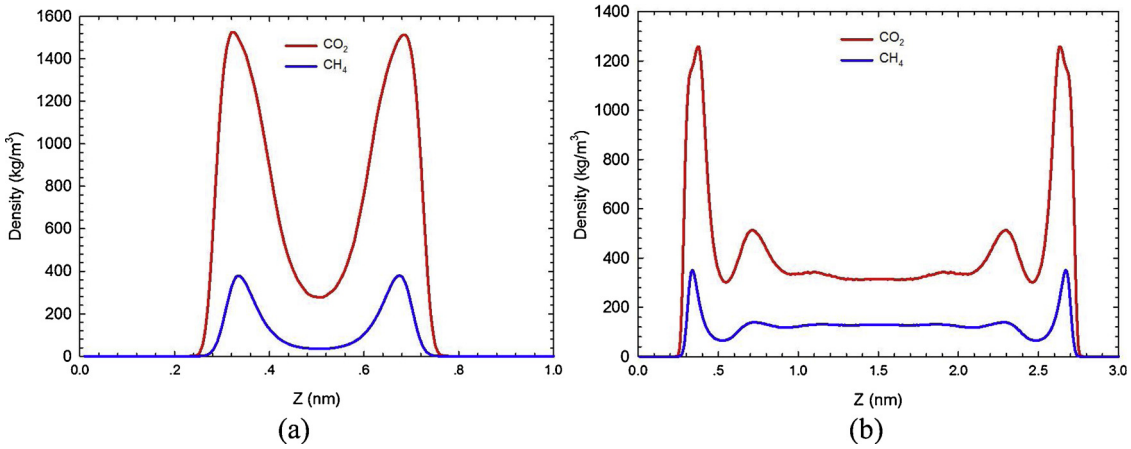


**Fig. 12.** Density profiles of $CO_2/CH_4$ (50.0 mol%:50.0 mol%) in the (a) 1-nm and (b) 3-nm kaolinite pores at 333.15 K and 350 bar.

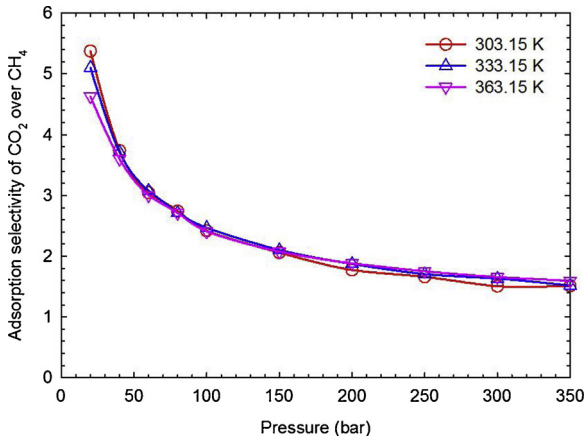


**Fig. 13.** Adsorption selectivity of $CO_2/CH_4$ (50.0 mol%:50.0 mol%) in the 3-nm illite pore.

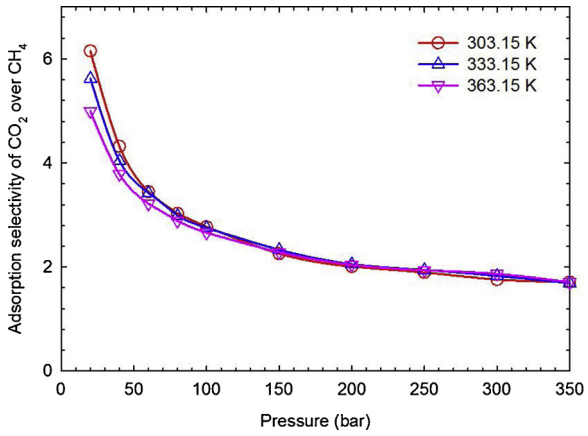


**Fig. 14.** Adsorption selectivity of $CO_2/CH_4$ (50.0 mol%:50.0 mol%) in the 3-nm montmorillonite pore.

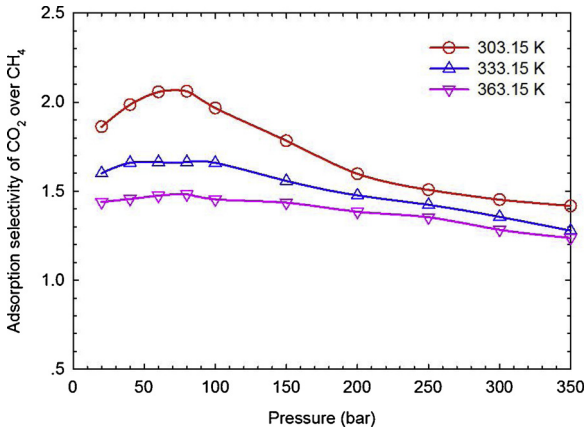


**Fig. 15.** Adsorption selectivity of $CO_2/CH_4$ (50.0 mol%:50.0 mol%) in the 3-nm kaolinite pore.
sequestration.

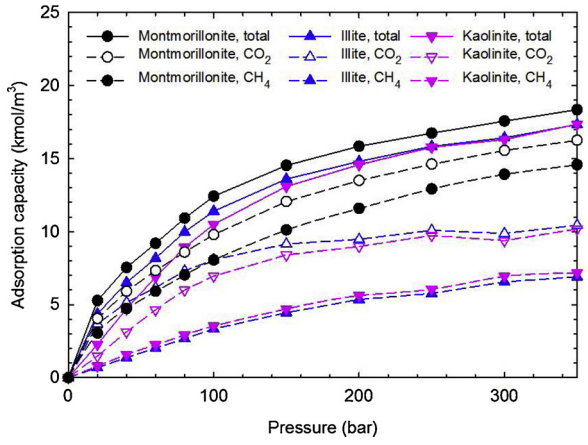


**Fig. 16.** Adsorption isotherms of $CO_2/CH_4$ (50.0 mol%:50.0 mol%) mixture and the individual adsorption of $CH_4$ and $CO_2$ in the 3-nm mineral pores at 303.15 K.

the optimum pressure on other materials for the adsorption selectivity of $CH_4$ and $CO_2$ [74]. The different adsorption selectivity of $CO_2$ over $CH_4$ on kaolinite results from the relatively higher adsorption capacity of $CO_2$ over $CH_4$ on the kaolinite mineral at the medium pressure conditions. During shale gas reservoir development, reservoir pressure decreases when $CH_4$ is produced from shale reservoirs. However, a large amount of adsorbed $CH_4$ are still left in the depleted shale gas reservoirs if no further exploitation was implemented. Based on our results, the injection pressure of $CO_2$ should be around 60 bar for kaolinite-rich shale, while the pressure for illite and montmorillonite-rich shales are around 30 bar, to realize the highest efficiency for $CH_4$ recovery and $CO_2$ sequestration in field applications.

Figs. 16–18 present the adsorption isotherms of $CO_2/CH_4$ (50.0 mol %:50.0 mol%) mixture and the individual adsorption of $CH_4$ and $CO_2$ in the 3-nm mineral pores. $CO_2/CH_4$ mixture has the adsorption capacity in the clay-mineral pores in the order of montmorillonite > illite >

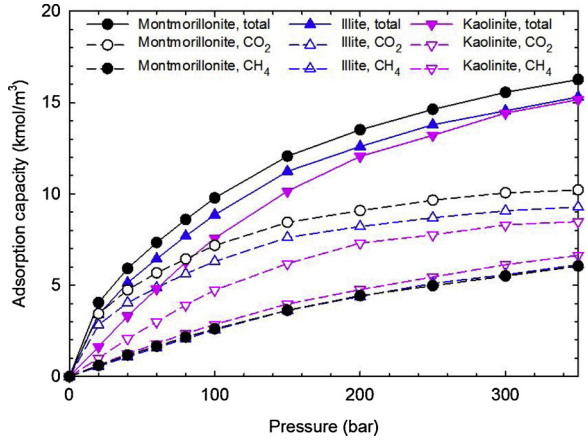


**Fig. 17.** Adsorption isotherms of $CO_2/CH_4$ (50.0 mol%:50.0 mol%) mixture and the individual adsorption of $CH_4$ and $CO_2$ in the 3-nm mineral pores at 333.15 K.

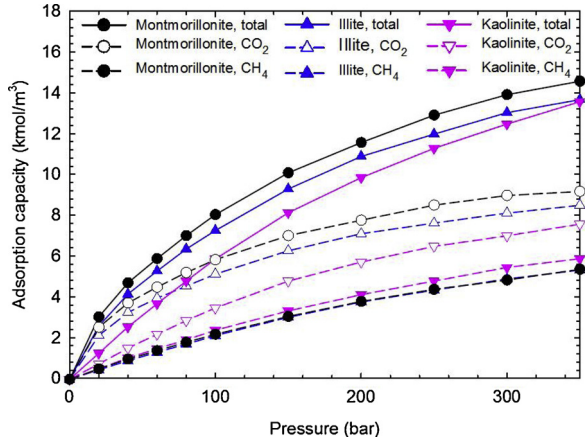


**Fig. 18.** Adsorption isotherms of $CO_2/CH_4$ (50.0 mol%:50.0 mol%) mixture and the individual adsorption of $CH_4$ and $CO_2$ in the 3-nm mineral pores at 363.15 K.

kaolinite. When pressure is low, illite exhibits stronger adsorption capacity to gas mixtures than kaolinite; however, as system pressure increases, adsorption capacity of the gas mixture on kaolinite approaches that on illite. Moreover, $CO_2$ has the highest adsorption capacity on the montmorillonite pore surface; on the contrary, montmorillonite shows the smallest adsorption capacity for $CH_4$. It validates our point that the montmorillonite-rich shale is the most ideal reservoir for $CO_2$ sequestration and $CO_2$ injection can achieve the best recovery efficiency of $CH_4$ in montmorillonite-rich shale reservoirs. By contrast, kaolinite has the smallest individual adsorption for $CO_2$ but the highest adsorption for $CH_4$, indicating that kaolinite-rich shales is unfavorable for $CH_4$ recovery and $CO_2$.

## 5. Conclusions

Adsorption of $CO_2/CH_4$ mixture are first measured on illite, montmorillonite and kaolinite minerals using the thermogravimetric method. GCMC simulations is then adopted to generate the three clay-mineral models and used to predict the $CO_2/CH_4$ adsorption; the GCMC simulation model is thus validated by comparing with the experimental data. Adsorption behavior of $CO_2/CH_4$ mixture is comprehensively investigated by analyzing the characteristics of fluid distributions in the clay-mineral pores. In addition, adsorption selectivity of $CO_2$ over $CH_4$ and the individual adsorption of $CO_2$ and $CH_4$ in the $CO_2/CH_4$ mixture are calculated to shed lights on the implication potentials of $CO_2$ injection for $CH_4$ recovery and $CO_2$ sequestration in the field applications. The detailed conclusions are summarized as follows:

- Our results show that $CH_4$ performs the highest adsorption on kaolinite, which is then followed by that on illite and montmorillonite. On the contrary, the adsorption capacity of $CO_2$ on clay minerals are calculated in the order of montmorillonite > illite ≈ kaolinite. That is, montmorillonite has the highest adsorption to $CO_2$ but the smallest adsorption capacity to $CH_4$, indicating that as for montmorillonite-rich shale, $CO_2$ injection could be a more efficient way for $CH_4$ recovery than that in the illite- and kaolinite-rich shale reservoirs;
- Adsorption of $CO_2/CH_4$ mixture on clay minerals is influenced by system temperature, pressure and pore size. Specifically, $CO_2$ adsorption on kaolinite is more sensitive to reservoir pressures compared to that on illite and montmorillonite. On the contrary, $CH_4$ adsorption on clay minerals is highly affected by reservoir pressures. It is inferred that $CO_2$ injection for $CH_4$ recovery is less efficient for kaolinite-rich shale. The maximum adsorption capacity of $CO_2$in the 3-nm montmorillonite and kaolinite pores is remarkably higher than that in the 1-nm pores. $CO_2$ is thereby superior in the large pores to that in the small pores for CH4 recovery. In addition, small pores are most probably dominated by the adsorbed gas in the clay nanopores, which are thereby the ideal space for $CO_2$ sequestration. As for clay-rich shale gas reservoirs, heavy attention should be taken on how to efficiently recover the adsorbed gas reserves from small pores;
- The adsorption selectivity of $CO_2$ over $CH_4$ is in the order of kaolinite < illite < montmorillonite; in addition, the adsorption selectivity for illite and montmorillonite decreases with the reservoir pressure, indicating that the injection pressure of $CO_2$ should be low enough for efficient $CO_2$ sequestration as well as $CH_4$ recovery. On the contrary, the maximum adsorption selectivity is observed for kaolinite; therefore, the injection pressure of $CO_2$ should be around the pressure where it has the maximum adsorption selectivity for kaolinite-rich shale.

Collectively, this work provides important insights into the mechanism of selective adsorption of $CH_4$ and $CO_2$ on tight clay-rich shale, which is beneficial to shale gas reservoir assessment and shale gas production optimization using $CO_2$ injection method. It is significantly economical for shale gas recovery in clay-rich shale reservoirs by optimizing $CO_2$ injection with the knowledge of the adsorption behavior of $CH_4$ and $CO_2$ on clay nanopores. In addition to $CH_4$, some heavier components, such as $C_2H_6$, $C_3H_8$, *etc.*, may also be dominating in shale gas. Thereby, future works are recommended to investigate the selective adsorption behavior between $CO_2$ and the heavier hydrocarbons. In addition, the adsorption sites may also play a key rule in affecting the adsorption behavior of $CO_2$ and $CH_4$ on shale. In future works, this topic should also be investigated.

## Author statement

Dr. Yueliang Liu and Dr Jian Hou have made substantial contributions to the concept and design of this work. Dr. Yueliang Liu also drafted this manuscript and Dr. Jian Hou revised it critically. Dr. Yueliang Liu and Dr. Jian Hou have approved the final version to be published.

## Declaration of Competing Interest

The author(s) declare(s) that there is no conflict of interests regarding the publication of this article.

## Acknowledgments

The first author acknowledges the financial supported by the China

Postdoctoral Science Foundation (ZX20190438) and the Special Support for Post-doc Creative Funding in Shandong Province to Dr. Y.L. Liu. The authors also appreciate the financial support of the National Science Foundation for Distinguished Young Scholars of China (51625403), the Important National Science and Technology Specific Projects of China (2016ZX05025-003) to Dr. J. Hou.

## Appendix A. Supplementary data

Supplementary material related to this article can be found, in the online version, at doi:https://doi.org/10.1016/j.jcou.2020.02.013.

## References

[1] A. Burnham, J. Han, C.E. Clark, M. Wang, J.B. Dunn, I. Palou-Rivera, Life-cycle greenhouse gas emissions of shale gas, natural gas, coal, and petroleum, Environ. Sci. Technol. 46 (2011) 619–627.
[2] J.D. Hughes, Energy: a reality check on the shale revolution, Nature 494 (2013) 307–308.
[3] K. Wu, Z. Chen, X. Li, Real gas transport through nanopores of varying cross-section type and shape in shale gas reservoirs, Chem. Eng. J. 281 (2015) 813–825.
[4] K. Falk, B. Coasne, R. Pellenq, F.J. Ulm, L. Bocquet, Subcontinuum mass transport of condensed hydrocarbons in nanoporous media, Nat. Commun. 6 (2015) 6949.
[5] J.B. Curtis, Fractured shale-gas systems, AAPG Bull 86 (11) (2002) 1921–1938.
[6] M. Chen, Y. Kang, T. Zhang, L. You, X. Li, Z. Chen, K. Wu, B. Yang, Methane diffusion in shales with multiple pore sizes at supercritical conditions, Chem. Eng. J. 334 (2018) 1455–1465.
[7] S.R. Etminan, F. Javadpour, B.B. Maini, Z. Chen, Measurement of gas storage processes in shale and of the molecular diffusion coefficient in kerogen, Int. J. Coal Geol. 123 (2014) 10–19.
[8] R. Heller, M. Zoback, Adsorption of methane and carbon dioxide on gas shale and pure mineral samples, J Unconven Oil Gas Resour 8 (2014) 14–24.
[9] S.L. Montgomery, D.M. Jarvie, K.A. Bowker, R.M. Pollastro, Mississippian Barnett Shale, Fort Worth basin, north-central Texas: gas-shale play with multi-trillion cubic foot potential, AAPG Bull 89 (2005) 155–175.
[10] X.C. Lu, F.C. Li, A.T. Watson, Adsorption measurements in Devonian shales, Fuel 74 (4) (1995) 599–603.
[11] X. Jiang, A review of physical modelling and numerical simulation of long-term geological storage of $CO_2$, Appl. Energy 88 (11) (2011) 3557–3566.
[12] C.M. White, D.H. Smith, K.L. Jones, A.L. Goodman, S.A. Jikich, R.B. LaCount, S.B. DuBose, E. Ozdemir, B.I. Morsi, K.T. Schroeder, Sequestration of carbon dioxide in coal with enhanced coalbed methane recovery a review, Energ Fuel 19 (3) (2005) 659–724.
[13] V. Vishal, T.N. Singh, P.G. Ranjith, Influence of sorption time in $CO_2$-ECBM process in Indian coals using coupled numerical simulation, Fuel 139 (2015) 51–58.
[14] R. Chatterjee, S. Paul, Classification of coal seams for coal bed methane exploitation in central part of Jharia coalfield, India-a statistical approach, Fuel 111 (2013) 20–29.
[15] N. Mac Dowell, P.S. Fennell, N. Shah, G.C. Maitland, The role of $CO_2$ capture and utilization in mitigating, Nat. Clim. Chang. 7 (2017) 243–249.
[16] W. Ampomah, R.S. Balch, M. Cather, R. Will, D. Gunda, Z. Dai, M.R. Soltanian, Optimal design of $CO_2$ storage and oil recovery under geological uncertainty, Appl. Energy 195 (2017) 80–92.
[17] Z. Dai, H. Viswanathan, R. Middleton, F. Pan, W. Ampomah, C. Yang, W. Jia, T. Xiao, S. Lee, B. McPherson, R. Balch, R. Grigg, M. White, $CO_2$ accounting and risk analysis for $CO_2$ sequestration at enhanced oil recovery sites, Environ. Sci. Technol. 50 (2016) 7546–7554.
[18] Z. Dai, P. Stauffer, J. Carey, R. Middleton, Z. Lu, J. Jacobs, L. Spangle, K. Hnottavange-Telleen, Pre-site characterization risk analysis for commercial-scale carbon sequestration, Environ. Sci. Technol. 48 (7) (2014) 3908–3915.
[19] B.C. Nuttall, C.F. Eble, J.A. Drahovzal, R.M. Bustin, Analysis of Devonian Black Shales in Kentucky for Potential Carbon Dioxide Sequestration and Enhanced Natural Gas Production, Report Kentucky Geological Survey/University of Kentucky, 2005.
[20] S.M. Kang, E. Fathi, R.J. Ambrose, I.Y. Akkutlu, R.F. Sigal, Carbon dioxide storage capacity of organic-rich shales, SPE J 16 (4) (2010) 842–855.
[21] S. Duan, M. Gu, X. Du, X. Xian, Adsorption equilibrium of $CO_2$ and $CH_4$ and their mixture on Sichuan Basin Shale, Energy Fuels 30 (3) (2016) 2248–2256.
[22] O. Ortiz Cancino, D.P. Pérez, M. Pozo, D. Bessieres, Adsorption of pure $CO_2$ and a $CO_2/CH_4$ mixture on a black shale sample: manometry and microcalorimetry measurements, J Petrol Sci Eng 159 (2017) 307–313.
[23] L. Ji, T. Zhang, K.L. Milliken, J. Qu, X. Zhang, Experimental investigation of main controls to methane adsorption in clay-rich rocks, Appl. Geochem. 27 (12) (2012) 2533–2545.
[24] T. Zhang, G.S. Ellis, S.C. Ruppel, K. Milliken, R. Yang, Effect of organic-matter type and thermal maturity on methane adsorption in shale-gas systems, Org. Geochem. 47 (2012) 120–131.
[25] D.J.K. Ross, R.M. Bustin, Shale gas potential of the lower jurassic gordondale member, northeastern british Columbia, Canada, Bull. Can. Petrol. Geol. 55 (1) (2007) 51–75.
[26] G.R.L. Chalmers, R.M. Bustin, Lower Cretaceous gas shales in northeastern British Columbia, part II: evaluation of regional potential gas resources, Bull. Can. Petrol. Geol. 56 (1) (2008) 22–61.
[27] A.L. Cheng, W.L. Huang, Selective adsorption of hydrocarbon gases on clays and organic matter, Org. Geochem. 35 (4) (2004) 413–423.
[28] X.C. Lu, F.C. Li, A.T. Watson, Adsorption measurements in Devonian shales, Fuel 74 (4) (1995) 599–603.
[29] D.J.K. Ross, R.M. Bustin, The importance of shale composition and pore structure upon gas storage potential of shale gas reservoirs, Mar. Petrol. Geol. 26 (6) (2009) 916–927.
[30] Y. Liu, J. Wilcox, Molecular simulation studies of $CO_2$ adsorption by carbon model compounds for carbon capture and sequestration applications, Environ. Sci. Technol. 47 (2012) 95–101.
[31] P. Psarras, R. Holmes, V. Vishal, J. Wilcox, Methane and $CO_2$ adsorption capacities of kerogen in the Eagle Ford shale from molecular simulation, Acc. Chem. Res. 50 (2017) 1818–1828.
[32] Z. Jin, A. Firoozabadi, Effect of water on methane and carbon dioxide sorption in clay minerals by Monte Carlo simulations, Fluid Phase Equilib. 382 (2014) 10–20.
[33] L. Huang, Z. Ning, Q. Wang, R. Qi, Y. Zeng, H. Qin, H. Ye, W. Zhang, Molecular simulation of adsorption behaviors of methane, carbon dioxide and their mixtures on kerogen: effect of kerogen maturity and moisture content, Fuel 211 (2018) 159–172.
[34] J. Zhang, K. Liu, M.B. Clennell, D.N. Dewhurst, M. Pervukhina, Molecular simulation of $CO_2$-$CH_4$ competitive adsorption and induced coal swelling, Fuel 160 (2015) 309–317.
[35] A. Kadoura, Sun S. Nair AKN, Adsorption of carbon dioxide, methane, and their mixture by montmorillonite in the presence of water, Microporous Mesoporous Mater. 225 (2016) 331–341.
[36] N. Yang, S. Liu, X. Yang, Molecular simulation of preferential adsorption of $CO_2$ over $CH_4$ in Na-montmorillonite clay material, Appl. Surf. Sci. 356 (2015) 1262–1271.
[37] M. Kazemi, A. Takbiri-Borujeni, Molecular dynamics study of carbon dioxide storage in carbon-based organic nanopores, Presented in the SPE Annual Technical Conference and Exhibition, 26-28 September, Dubai, UAE (2016).
[38] Y. Kurniawan, S.K. Bhatia, V. Rudolph, Simulation of binary mixture adsorption of methane and $CO_2$ at supercritical conditions in carbons, AIChE J. 52 (3) (2006) 957–967.
[39] Q. Yuan, X. Zhu, K. Lin, Y.P. Zhao, Molecular dynamics simulations of the enhanced recovery of confined methane with carbon dioxide, Phys. Chem. Chem. Phys. 17 (2015) 31887–31893.
[40] L. Brochard, M. Vandamme, R.J.M. Pellenq, T. Fen-Chong, Adsorption-induced deformation of microporous materials: coal swelling induced by $CO_2$-$CH_4$ competitive adsorption, Langmuir 28 (2012) 2659–2670.
[41] X. Wang, Z. Zhai, X. Jin, S. Wu, J. Li, L. Sun, X. Liu, Molecular simulation of $CO_2$/$CH_4$ competitive adsorption in organic matter pores in shale under certain geological conditions, Petrol. Explor. Dev. 43 (5) (2016) 841–848.
[42] X. Lu, D. Jin, S. Wei, M. Zhang, Q. Zhu, X. Shi, Z. Deng, W. Guo, W. Shen, Competitive adsorption of a binary $CO_2$-$CH_4$ mixture in nanoporous carbons: effects of edge-functionalization, Nanoscale 7 (3) (2015) 1002–1012.
[43] X. Liu, X. He, N. Qiu, X. Yang, Z.Y. Tian, M. Li, Y. Xue, Molecular simulation of $CH_4$, $CO_2$, $H_2O$ and $N_2$ molecules adsorption on heterogeneous surface models of coal, Appl. Surf. Sci. 389 (2016) 894–905.
[44] H. Sun, H. Zhao, N. Qi, Y. Li, Molecular insights into the enhanced shale gas recovery by carbon dioxide in kerogen slit nanopores, J Phys Chem C 121 (18) (2017) 10233–10241.
[45] S. Kong, Li K. H X, X. Song, Adsorption/desorption isotherms of $CH_4$ and $C_2H_6$ on typical shale samples, Fuel 255 (2019) 115632.
[46] Y. Liu, J. Hou, C. Wang, Absolute adsorption of $CH_4$ on shale with the simplified local-density theory, SPE J. 25 (1) (2020) 212–225.
[47] W.A. Deer, R.A. Howie, J. Zussman, An Introduction to the Rock Forming Minerals, Longman, London, 1996.
[48] M. Szczerba, A. Derkowski, A.G. Kalinichev, J. Środoń, Molecular modeling of the effects of 40Ar recoil in illite particles on their K-Ar isotope dating, Geochim. Cosmochim. Acta 159 (2015) 162–176.
[49] C.I. Sainz-Diaz, E.J. Palin, M.T. Dove, A. Hernandez-Laguna, Monte Carlo simulations of ordering of Al, Fe, and Mg cations in the octahedral sheet of smectites and illites, Am. Mineral. 88 (7) (2003) 1033–1045.
[50] R. Wardle, G.W. Brindley, Crystal-structures of pyrophyllite, 1Tc, and of its dehydroxylate, Am. Mineral. 57 (5–6) (1972) 732–750.
[51] H. Wang, X. Wang, X. Jin, D. Cao, Molecular dynamics simulation of diffusion of shale oils in montmorillonite, J Phys Chem C 120 (2016) 8986–8991.
[52] M. Chávez-Páez, K.V. Workum, L.D. Pablo, J.J.D. Pablo, Monte Carlo simulations of Wyoming sodium montmorillonite hydrates, J. Chem. Phys. 114 (2001) 1405–1413.
[53] C.M. Tenney, R.T. Cygan, Molecular simulation of carbon dioxide, brine, and clay mineral interactions and determination of contact angles, Environ Sci Tech 48 (2014) 2035–2042.
[54] M.G. Martin, J.I. Siepmann, Transferable potentials for phase equilibria.1. United-atom description of n-alkanes, J. Phys. Chem. B 102 (14) (1998) 2569–2577.
[55] R.T. Cygan, J.J. Liang, A.G. Kalinichev, Molecular models of hydroxide, oxyhydroxide, and clay phases and the development of a general force field, J. Phys. Chem. B 108 (2004) 1255–1266.
[56] H.A. Lorentz, Nachtrag zu der Abhandlung: Ueber die Anwendung des Satzes vom Virial in der kinetischen Theorie der Gase, Ann. Phys. 248 (4) (1881) 660–661.
[57] Z. Jin, A. Firoozabadi, Effect of water on methane and carbon dioxide sorption in clay minerals by Monte Carlo simulations, Fluid Phase Equilib. 382 (2014) 10–20.
[58] P.S. Crozier, R.L. Rowley, E. Spohr, D. Henderson, Comparison of charged sheets

and corrected 3D Ewald calculations of long-range forces in slab geometry electrolyte systems with solvent molecules, J. Chem. Phys. 112 (2000) 9253–9257.
[59] Y. Liu, H.A. Li, Y. Tian, Z. Jin, H. Deng, Determination of the absolute adsorption/desorption isotherms of $CH_4$ and n-$C_4H_{10}$ on shale from a nano-scale perspective, Fuel 218 (2018) 67–77.
[60] X. Lu, D. Jin, S. Wei, M. Zhang, Q. Zhu, X. Shi, Z. Deng, W. Guo, W. Shen, Competitive adsorption of a binary $CO_2$-$CH_4$ mixture in nanoporous carbons: effects of edge-functionalization, Nanoscale 7 (2015) 1002–1012.
[61] Y. Tian, C. Yan, Z. Jin, Characterization of methane excess and absolute adsorption in various clay nanopores from molecular simulation, Sci. Rep. 7 (2017) 12040.
[62] T. Zhang, G.S. Ellis, S.C. Ruppel, K. Milliken, R. Yang, Effect of organic-matter type and thermal maturity on methane adsorption in shale-gas systems, Org. Geochem. 47 (2012) 120–131.
[63] Y. Kurniawan, S.K. Bhatia, V. Rudolph, Simulation of binary mixture adsorption of methane and $CO_2$ at supercritical conditions in carbons, AIChE J. 52 (3) (2006) 957–967.
[64] Y. Liu, J. Wilcox, Molecular simulations of $CO_2$ adsorption in micro- and mesoporous carbons with surface heterogeneity, Int. J. Coal Geol. 104 (2012) 83–95.
[65] J.S. Bae, T.X. Nguyen, S.K. Bhatia, Pore accessibility of $Ti_3SiC_2$-derived carbons, Carbon 68 (2014) 531–541.
[66] Y. Liu, Z. Jin, H. Li, Comparison of Peng-Robinson equation of state with capillary pressure model with engineering density-functional theory in describing the phase behavior of confined hydrocarbons, SPE J 23 (05) (2018) 1784–1797.
[67] T.X. Nguyen, S.K. Bhatia, Determination of pore accessibility in disordered nanoporous materials, J Phys Chem C 111 (5) (2007) 2212–2222.
[68] J.S. Bae, S.K. Bhatia, V. Rudolph, P. Massarotto, Pore accessibility of methane and carbon dioxide in coals, Energ Fuel 23 (6) (2009) 3319–3327.
[69] T.X. Nguyen, S.K. Bhatia, Kinetic restriction of simple gases in porous carbons: transition-state theory study, Langmuir 24 (1) (2008) 146–154.
[70] J.S. Bae, S.K. Bhatia, High-pressure adsorption of methane and carbon dioxide on coal, Energ Fuel 20 (6) (2006) 2599–2607.
[71] L. Huang, Z. Ning, Q. Wang, W. Zhang, Z. Cheng, X. Wu, H. Qin, Effect of organic type and moisture on $CO_2$/$CH_4$ competitive adsorption in kerogen with implication, ACS Appl. Energy Mater. 210 (2018) 28–43.
[72] Y. Liu, J. Hou, Investigation on the potential relationships between geophysical properties and $CH_4$ adsorption in a typical shale gas reservoir, Energy Fuels 33 (2019) 8354–8362.
[73] S. Bachu, Sequestration of $CO_2$ in geological media in response to climate change: road map for site selection using the transform of the geological space into the $CO_2$ phase space, Energy Convers. Manage. 43 (1) (2002) 87–102.
[74] R.B. Vieira, P.A.S. Moura, E. Vilarrasa-García, D.C.S. Azevedo, H.O. Pastore, Polyamine-grafted magadiite: high $CO_2$ selectivity at capture from $CO_2$/$N_2$ and $CO_2$/$CH_4$ mixtures, J. $CO_2$ Util. 23 (2018) 29–41.